

A methodology for generating four-dimensional arterial spin labeling MR angiography virtual phantoms

Renzo Phellan^a, Thomas Lindner^b, Michael Helle^c, Alexandre X. Falcão^d,
Thomas W. Okell^e, Nils D. Forkert^a

^a*Department of Radiology and Hotchkiss Brains Institute - University of Calgary -
Calgary - AB - Canada.*

^b*Clinic for Radiology and Neuroradiology - University Medical Center Schleswig-Holstein
- Kiel - Germany*

^c*Philips Technologie GmbH - Innovative Technologies - Hamburg - Germany*

^d*Laboratory of Image Data Science - Institute of Computing - University of Campinas -
Campinas - SP - Brazil*

^e*Wellcome Centre for Integrative Neuroimaging - FMRIB - Nuffield Department of
Clinical Neurosciences - University of Oxford - Oxford - United Kingdom*

Abstract

Four-dimensional arterial spin labeling magnetic resonance angiography (4D ASL MRA) is a non-invasive medical imaging modality that can be used for anatomical and hemodynamic analysis of the cerebrovascular system. However, it generates a considerable amount of data, which is tedious to analyze visually. As an alternative, medical image processing methods can be used to process the data and present measurements of the geometry and blood flow in the cerebrovascular system to the user, such as vessel radius, tortuosity, blood flow volume, and transit time. Nevertheless, evaluating medical image processing methods developed for this modality requires annotated data, which can be time-consuming and expensive to obtain. Alternatively, virtual simulations are a faster and less expensive option that can be used for initial evaluation of image processing methods. The present work proposes a methodology for generating annotated 4D ASL MRA virtual phantoms, in different scenarios with different acquisition parameter settings. In each scenario, the phantoms are generated using real cerebrovascular geometries of healthy volunteers, where blood flow is simulated according to a mathematical model specifically designed to describe the signal observed in 4D ASL MRA images. Realistic noise is added using an homomorphic approach, designed to replicate noise characteristic of multi-coil acquisitions. In order to

exemplify the utility of the phantoms, they are used to evaluate the accuracy of a method to estimate blood flow parameter values, such as relative blood volume and transit time, in different scenarios. The estimated values are then compared to its corresponding virtual ground-truth values. The accuracy of the results is ranked according to the average absolute error. The results of the experiments show that blood flow parameters can be more accurately estimated when blood is magnetically labeled for longer periods of time and when the datasets are acquired with higher temporal resolution. In summary, the present work describes a methodology to create annotated virtual phantoms, which represent a useful alternative for initial evaluation of medical image processing methods for 4D ASL MRA images.

Keywords:

Angiography, Cerebrovascular imaging, Arterial spin labeling, Blood flow analysis, Phantom models.

1. Introduction

Cerebrovascular diseases are among the top ten causes of death according to the global report published by the World Health Organization, with increasing prevalence over the last fifteen years (Department of information, evidence and research of the World Health Organization, 2017). Four-dimensional arterial spin labeling magnetic resonance angiography (4D ASL MRA) is a non-invasive medical imaging modality that can be used for investigation of the anatomical structure and blood flow of the cerebrovascular system at high spatial and temporal resolution (Robson et al., 2010). Therefore, this rather new MRA imaging technique has high potential to support diagnosis, treatment planning, and follow-up assessment of cerebrovascular diseases, such as aneurysms, arteriovenous-malformations, stenosis, and stroke. However, 4D ASL MRA generates a considerable amount of data, which is time-consuming and tedious to analyze directly. A solution to this problem is using medical image processing methods to process the data, in order to extract the information contained in 4D ASL MRA images (Phellan et al., 2018b). This information includes geometric measurements of the vascular system, such as vessel radius, tortuosity, and density, and hemodynamic measurements, e.g. blood flow volume and transit time.

Developing and evaluating the novel image processing methods for 4D ASL MRA usually requires annotated datasets, with geometric and blood

flow ground-truth values. These datasets are time-consuming and expensive to obtain (Hamarneh and Jassi, 2010). Alternatively, virtual phantoms are a faster and less expensive option for initial evaluation of medical image processing methods. Some examples include the BrainWeb database (Cocosco et al., 1997), which contains simulated brain magnetic resonance images with configurable parameter settings. Additionally, the software VascuSynth (Hamarneh and Jassi, 2010) allows the creation of volumetric images of a vascular tree with corresponding ground-truth geometries, but no blood flow data. Finally, a simulation of blood flow in the cerebral venous system was proposed as part of the VIVABRAIN project (Miraucourt et al., 2017). In this case, subject-specific geometries are used as the basis for blood flow simulation employing the Navier-Stokes equations for incompressible viscous fluid. Currently, to the best of our knowledge, no virtual phantoms are available to evaluate medical image processing methods specifically for 4D ASL MRA series.

The first objective of the present study is to present a methodology to create annotated virtual phantoms of 4D ASL MRA series from subject-specific geometries, based on a mathematical model of the blood flow specifically designed to describe the temporal signal measured by this imaging modality (Okell et al., 2010). Additionally, in order to achieve a realistic simulation, noise is added using an homomorphic approach (Aja-Fernández et al., 2015), designed to replicate noise characteristic of multi-coil acquisitions. The second objective is to compare the accuracy of a blood flow parameter estimation method using phantoms generated with different acquisition parameters. The source code developed as part of this project to generate the phantoms is available online (Phellan, 2019).

2. Materials and Methods

2.1. Materials

Local institutional ethics committee (Ärztchamber Schleswig-Holstein and Calgary Health Regional Ethic Board) approval was obtained and all subjects provided written informed consent consistent with the Declaration of Helsinki prior to study participation.

3D multi-slab time-of-flight (TOF) MRA images were acquired from ten volunteers using a Philips Achieva 3T MRI scanner (Philips Healthcare, Best, The Netherlands), with a standard 32-channel head coil. Only healthy subjects without any history of cerebrovascular or neurological diseases were

included. Each TOF MRA image is composed of 171 slices with 512×512 voxels, with voxel size $0.41 \times 0.41 \times 0.70 \text{ mm}^3$. A flow compensated readout was used, with SENSE factor 2, $TR = 20 \text{ ms}$, $TE = 3.45 \text{ ms}$, flip angle 20° , and half scan factor 0.7. The total scan time was 6:39 minutes. TOF MRA images can capture the subjects cerebrovascular geometry with higher spatial resolution than 4D ASL MRA, but they do not contain any temporal data.

Additionally, corresponding 4D ASL MRA series were acquired from the same volunteers using the same scanner during the same imaging session, for qualitative comparison of the proposed virtual phantom datasets. Each 4D ASL MRA series contains six three-dimensional control/labeled image pairs that display the passage of magnetically labeled blood through the cerebrovascular system, with a temporal resolution of 120 ms . Each image contains 120 slices of 224×224 voxels, with voxel size $0.94 \times 0.94 \times 1.0 \text{ mm}^3$, from the base of the neck to the top of the head. Image acquisition was performed using pseudo-continuous ASL and a Look-Locker readout to speed up the process. A T1-Turbo Field Echo (TFE) scan was employed, with TFE factor 16, SENSE factor 3, $TR = 7.7 \text{ ms}$, $TE = 3.7 \text{ ms}$, flip angle 10° , and half scan factor 0.7. The blood was magnetically labeled for 300 ms . The SENSE factor was only applied in the phase-encoding direction because extensive pulsation artifacts were noted in case of application in the through-slice directions. The total scan time was 5 minutes.

Figure 1 shows the proposed methodology to create 4D ASL MRA virtual phantoms, described in more detail in the following. Because of the higher spatial resolution of TOF MRA images compared to 4D ASL MRA series, blood flow parameter values are initially simulated in TOF MRA space and then resampled to 4D ASL space taking partial volume effects into account. The real 4D ASL MRA images acquired for this work are only used as a reference, and they are not required to create the phantoms.

2.2. Pre-processing

As this work focuses on arteries in the brain, all ten TOF MRA images acquired from healthy volunteers are skull-stripped using a fully automatic segmentation algorithm (Forkert et al., 2009). Then, the cerebrovascular system is segmented in the TOF MRA images using a validated automatic method (Forkert et al., 2013), generating ten binary segmentations. For creation of the 4D ASL MRA virtual phantoms, the ten TOF MRA binary vessel segmentations are divided into three main vascular territories, depending on

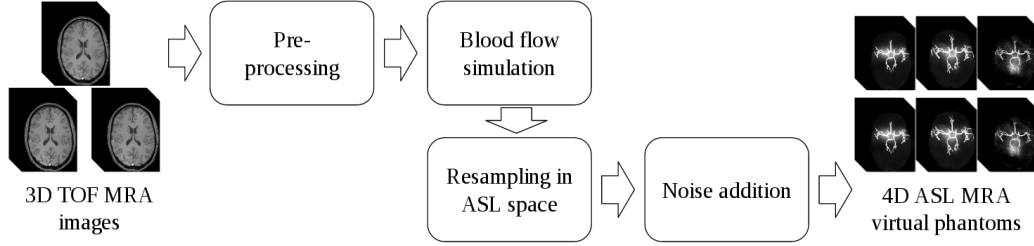


Figure 1: Diagram of the proposed methodology for 4D ASL MRA virtual phantoms generation.

the main feeding artery: left internal carotid artery (LICA), right internal carotid artery (RICA), or basilar artery (BA). For simplicity reasons, it is assumed that only one artery feeds each territory, so that there is no mixing of blood originating from different arteries. This is a reasonable assumption for healthy subjects (Okell et al., 2010), and it simplifies the computational calculations described below. The separation of the full arterial tree into the three main vessel territories is performed in this work using the image foresting transform algorithm (IFT) (Falcão et al., 2004). The IFT is a graph-based path optimization algorithm that requires the manual selection of three seed voxels at the origin of each main artery territory (LICA, RICA, and BA), which can be seen in Figure 2A. Then, the IFT algorithm assigns each non-seed voxel in the binary segmentation to a feeding artery by identifying the most closely connected seed voxel (i.e., the one that is associated with the minimum path length). Figure 2 shows 3D visualizations of the resulting images after applying the IFT algorithm to identify the LICA, RICA, and BA vessel territories. As it can be noted, the IFT generates both, a main vessel territory map (Figure 2B) and a map that displays the length of the path from each manually selected seed voxel in a main feeding artery to every other voxel that belongs to this artery (Figure 2C).

The last pre-processing step aims at defining blood flow velocities for the extracted vessels. Since no velocity measurements such as phase-contrast MRA datasets were available, population-based normative values were used in this work instead. Therefore, the three main vessel territories (LICA, RICA, and BA) were further manually subdivided into the left and right posterior cerebral arteries (LPCA and RPCA), left and right middle cerebral arteries (LMCA and RMCA), and anterior cerebral artery (ACA) (Figure 2D). After this step, population-based blood flow values were randomly

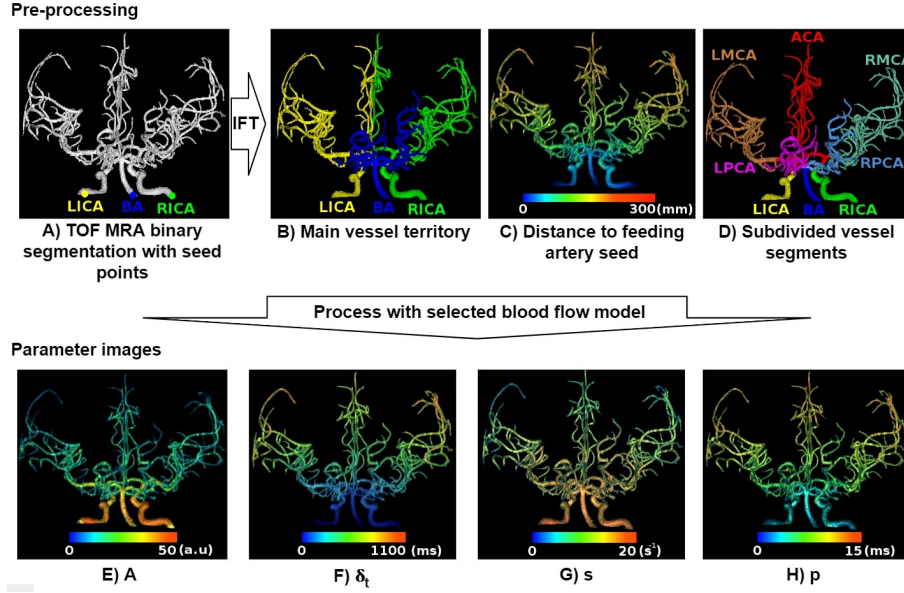


Figure 2: 3D visualizations of the pre-processing steps and resulting blood flow parameter images. A is a scaling factor, proportional to the blood volume; δ_t is the blood transit time from the labeling plane to any artery; and s and p are the sharpness and time-to-peak of the distribution that models the dispersion of blood as it flows through the cerebrovascular system.

139 selected within the ranges reported by Zarrinkoob et al. (Zarrinkoob et al.,
 140 2015), and assigned to the LICA, RICA, and BA sections. In order to con-
 141 serve the mass of blood in the system, the flow is then distributed to the
 142 LPCA, RPCA, LMCA, RMCA, and ACA, according to the proportions de-
 143 scribed by Zarrinkoob et al. (Zarrinkoob et al., 2015), assuming no mixture
 144 of blood. Finally, the blood flow is distributed equally at every branching
 145 point within the previously listed artery sections. This is a reasonable as-
 146 sumption considering that no flow measurements have been reported at this
 147 level of detail, due to the considerable inter-subject variability of the small
 148 vessels in the cerebrovascular system.

149 Once the blood flow values are assigned to every segment of the cere-
 150 brovascular system, the blood flow velocities V are estimated according to
 151 the formula shown in Equation 1, where F denotes blood flow, and A the
 152 cross sectional area of a vascular segment. The feasibility of the resulting
 153 velocities is automatically verified by comparison to corresponding reference
 154 values and ranges reported by MacDonald et al. (MacDonald and Frayne,

2015).

$$F = A \times V \quad (1)$$

2.3. Parameter and blood flow images

After identification of the vascular segments, the mathematical model proposed by Okell et al. (Okell et al., 2010) specifically developed for 4D ASL MRA image series is used to simulate the time curve S representing the signal of magnetically labeled blood flowing through the cerebrovascular system for each voxel. This model is selected because it is one of the few in the scientific literature that describes the 4D ASL MRA measured signal of labeled blood as it flows through the brain arteries, before reaching the capillaries and perfusing the brain tissue. The model is presented in Equation 2.

$$S(u, t) = \int_{t-\delta_t-\tau}^{t-\delta_t} A(u) dt_d D(u, t_d) T(\delta_t, t_d) R(t) \quad (2)$$

$$D(u, t_d) = \begin{cases} s(\Gamma(1 + ps))^{-1} \exp(-st_d)(st_d)^{ps} & \text{if } st_d > 0, ps > -1 \\ 0 & \text{otherwise} \end{cases} \quad (3)$$

$$T(\delta_t, t_d) = \exp(-(\delta_t + t_d)/T_{1b}) \quad (4)$$

$$R(t) = \cos(\alpha)^{(t-t_0)/TR} \sin(\alpha) \quad (5)$$

Here, $S(u, t)$ is the signal in voxel u , at time t , τ is the magnetic blood labeling time, δ_t is the blood transit time from the labeling plane to the voxel u , and t_d is the additional time delay caused by dispersion of the blood before reaching the voxel u . The term $A(u)$ is a scaling factor, which is proportional to the blood volume. This last term includes a calibration factor S_0 in its formulation, which accounts for the equilibrium magnetization of blood M_{0b} .

The term $D(u, t_d)$ in Equation 3 is a distribution that models the dispersion of labeled blood. It depends on the parameters s and p , which control the sharpness and time to peak of the distribution, respectively. The gamma function (Γ) is used to normalize the distribution. The term $T(\delta_t, t_d)$ in Equation 4 models the signal attenuation due to T_1 decay, where T_{1b} is the longitudinal relaxation time of arterial blood. The value of T_{1b} at 3T is estimated as $1664 \pm 14 \text{ ms}$ (Lu et al., 2004). Finally, the term $R(t)$ (Equation 5) accounts for the signal attenuation due to imaging radiofrequency pulses applied to the labeled blood as it reaches its destination. The parameter α

180 corresponds to the flip angle associated to the imaging pulse, t_0 is the time
 181 at which the first imaging pulse is applied, and TR is the repetition time.
 182 The model assumes that all transverse magnetization is spoiled at the end
 183 of every TR , so that the longitudinal magnetization is reduced by a factor of
 184 $\cos(\alpha)$ with every pulse. In this work, the simplified version of the term $R(t)$,
 185 proposed by Okell et al. (Okell et al., 2010), is used under the assumption
 186 that the imaging region comprises only anatomical structures distal to the
 187 labeling plane. Finally, the term $\sin(\alpha)$ accounts for the amount of transverse
 188 magnetization generated from a given amount of longitudinal magnetization.
 189 A summary of the terms and parameters used for blood flow simulation is
 190 presented in Table 1.

Term	Description
u	Voxel being analyzed.
t	Time transurred since the start of the acquisition process.
$S(u, t)$	Signal in voxel u , at time t .
τ	Time the blood is magnetically labeled.
δ_t	Blood transit time from the labeling plane to the voxel u .
t_d	Time delay caused by dispersion of the blood.
$A(u)$	Scaling factor, proportional to the blood volume in voxel u .
$D(u, t_d)$	Distribution that models the dispersion of labeled blood.
s	Sharpness of $D(u, t_d)$.
p	Time-to-peak of $D(u, t_d)$.
$\Gamma(x)$	Gamma function.
$T(\delta_t, t_d)$	Signal attenuation due to T_1 decay.
T_{1b}	Longitudinal relaxation time of arterial blood.
$R(t)$	Signal attenuation due to imaging radiofrequency pulses.
α	Flip angle.
t_0	Time at which the first imaging pulse is applied.
TR	Repetition time.

Table 1: Descriptions of the terms and parameters used for blood flow simulation.

191 To calculate the temporal signal curve $S(u, t)$ for each voxel u at time t in
 192 a 4D ASL MRA series, the following parameters must be known or estimated:
 193 $A(u)$, δ_t , s , p , τ , T_{1b} , α , t_0 , and TR . The first four are blood flow parameters,
 194 where the volume $A(u)$ is assumed to be proportional to the square of the
 195 artery radius, according to the Hagen-Poiseuilles law (Hagen, 1839; Poiseuille,

1844). The radius of each artery is obtained from the subject-specific artery geometries by using an image processing algorithm that calculates the distance of every voxel in the skeleton of an artery to the closest non-artery voxel. The skeleton values are then propagated within each voxel's region of influence, according to a Voronoi map (Phellan and Forkert, 2017). The largest artery in a binary segmentation is assigned the maximum relative volume value selected for the simulations, and the other arteries are assigned relative volume values proportional to the square of their radius over the square of the largest artery radius. The blood arrival time δ_t is calculated for each voxel by dividing the path length from the distance map by the average blood flow velocity along the path from the corresponding seed voxel. The parameters s and p vary inversely proportionally and proportionally to the path length indicated in the distance map, respectively (Okell et al., 2010). For automatic definition of s and p for every artery voxel, the artery voxels with path length value of 0 in the distance map are assigned predefined maximum s and minimum p values of 15 s^{-1} and 0 ms , respectively, and the artery voxels with maximum path length value are assigned predefined minimum s and maximum p values of 0 s^{-1} and 15 ms , respectively. For all other artery voxels, s and p values are interpolated by considering their corresponding path length. The minimum and maximum s and p values are obtained from the results of the experiments reported by Okell et al. (Okell et al., 2010). Figure 2 shows an example of the parameter values $A(u)$, δ_t , s , and p (Figures 2E, 2F, 2G, and 2H respectively) for a whole cerebrovascular system. The remaining five variables are image acquisition parameters (τ , T_{1b} , α , t_0 , and TR), which are defined according to the different scenarios evaluated in this work described below.

The simulated 4D ASL MRA datasets and the corresponding blood flow parameter images, generated in TOF MRA space are resampled into the 4D ASL MRA space by using linear interpolation, which adds partial volume effects to the process. Figure 3 shows a simulated 4D ASL MRA series. Additionally, to generate vascular ground-truth segmentations for the resampled 4D ASL MRA series, a temporal maximum intensity projection was calculated and thresholded at a low signal intensity value $th = 0.0001$. This leads to a precise segmentation as no noise artefacts are present in the simulated and downsampled images yet.

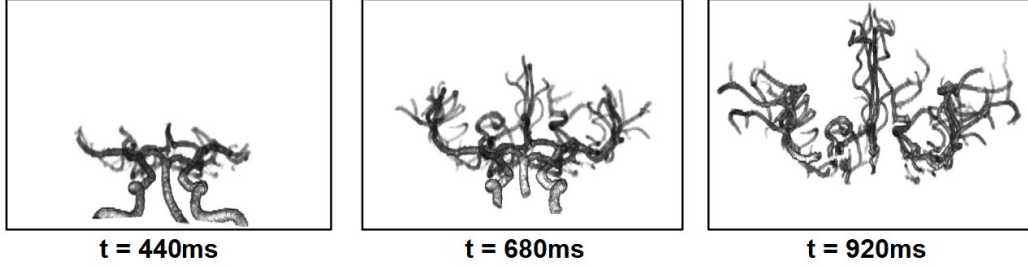


Figure 3: 3D renderings of three images of the simulated 4D ASL MRA series, for $t = 440$, 680 , and 920 ms (scenario 1).

2.4. Noise addition

The real 4D ASL MRA datasets used as a reference to create the simulated datasets were acquired using a standard 32-channel head coil, with SENSE reconstruction. In this case, the noise present in the magnitude of the signal can be assumed to follow a Rician distribution (Aja-Fernández et al., 2014). Additionally, the variance of the noise (σ^2) is expected to vary locally in the image as a consequence of the multi-coil acquisition (Aja-Fernández et al., 2015).

A homomorphic approach (Aja-Fernández et al., 2015) was used in this work in order to replicate the Rician noise from real datasets in the simulated datasets. The main advantage of this approach is that it does not require additional information regarding the acquisition of the datasets to estimate the noise parameters, such as multiple acquisitions, biophysical models, or coil sensitivity estimations (Aja-Fernández et al., 2014).

Practically, the freely available implementation described by Kiepas et al. (Kiepas and Sieradzki, 2015) was applied in this work in a slice-by-slice manner to each control/labeled pair of images of a real dataset. The algorithm computes a map with the noise variance (σ^2) for each voxel of an image that belongs to a 4D ASL MRA dataset. After this, noise images are generated for each control and label image and simulated time point using the determined local noise variance for each voxel. The generated noise images of each control and label image pair are subtracted and the resulting noise image is added to the corresponding simulated 4D ASL image. Figure 4 shows an example of a simulated 4D ASL MRA dataset, with added noise.

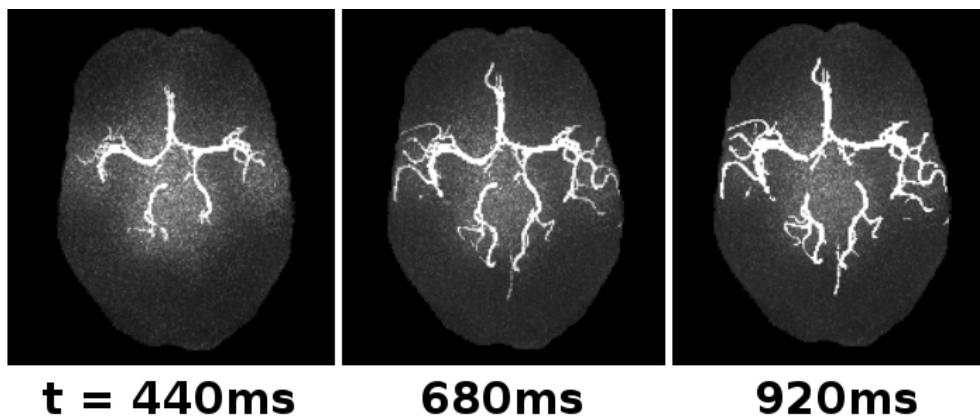


Figure 4: Maximum intensity projections of 30 contiguous slices of three images of the simulated 4D ASL MRA series, for $t = 440$, 680 , and 920 ms (scenario 1).

255 3. Experiments

256 In order to exemplify the utility of the virtual phantoms, they are used to
 257 evaluate the accuracy of a blood flow parameter estimation method. Given
 258 the degree of freedom of the 4D ASL MRA phantoms with respect to the
 259 acquisition parameters, twelve scenarios are generated, as described below,
 260 for which the blood flow parameter estimation method is evaluated.

261 3.1. Simulation Scenarios

262 Twelve different 4D ASL MRA image series were generated for each of
 263 the ten subjects available using different acquisition parameter settings for
 264 the simulations. More precisely, the voxel-wise blood flow parameters $A(u)$,
 265 δ_t , s , and p were kept the same in all scenarios, but different values were
 266 used for the acquisition parameters τ , α , t_0 , and TR (Table 2). The tempo-
 267 ral resolution of the simulated series (r) is also reported, together with the
 268 different time intervals when images are acquired, and the number of images
 269 (n) within those intervals (see Table 2). T_{1b} has a constant value, as all images
 270 are simulated to be acquired at a magnetic field strength of 3T.

271 It is important to notice that the temporal resolution used in each sce-
 272 nario is restricted by the configuration of acquisition parameters used. All
 273 evaluated scenarios are feasible since configurations reported in the scientific
 274 literature were used for this (Kopeinigg and Bammer, 2014; Okell et al., 2010;
 275 Phellan et al., 2018b).

Scen.	r (ms)	τ (ms)	α (°)	t_0 (ms)	TR (ms)	Interval (ms)	n
1	35	300	10	320	7.5	320–915	18
2	55	300	10	320	7.5	320–925	12
3	90	300	10	320	7.5	320–950	8
4	120	300	10	320	7.5	320–920	6
5	35	1000	20	1015	18	1015–2065	31
6	55	1000	20	1015	18	1015–2060	20
7	90	1000	20	1015	18	1015–2095	13
8	120	1000	20	1015	18	1015–2095	10
9	35	3000	6	3000	7.2	3000–5590	75
10	55	3000	6	3000	7.2	3000–5585	48
11	90	3000	6	3000	7.2	3000–5520	29
12	120	3000	6	3000	7.2	3000–5520	22

Table 2: Acquisition parameter values and times in each scenario, based on configuration described by Phellan et al. (2018b) (scenarios 1 to 4), Okell et al. (2010) (scenarios 5 to 8), and Kopeinigg and Bammer (2014) (scenarios 9 to 12).

276 3.2. Blood flow parameter estimation method

277 A common method for blood flow parameter estimation is to fit a math-
278 ematical model containing the parameters to be estimated to the observed
279 signal over time, for each voxel that belongs to an artery of interest in the
280 brain. In this work, the same model used to generate the phantoms (Okell
281 et al., 2010) is selected for curve fitting to the simulated 4D ASL MRA sig-
282 nal. It should be noted that the signal present in the 4D ASL MRA virtual
283 phantoms has been affected by partial volume effects and Rician noise ad-
284 dition, so that using the same model for blood flow parameter estimation is
285 not expected to lead to the original parameter values.

286 A typical approach to fit a hemodynamic model function to discrete con-
287 centration time curves for hemodynamic analysis is to use an optimization
288 method, e.g. by minimizing the sum of squared differences between the mea-
289 sured curve and the optimized model using the Powell algorithm or other
290 algorithms (Forkert et al., 2011). In this work, the blood flow parameter
291 values are optimized using the Multi-Scale Parameter Search (MSPS) algo-
292 rithm, which has been proven to be suitable for medical image processing
293 tasks (Phellan et al., 2018b; Ruppert et al., 2017).

294 The MSPS algorithm requires a set of scales for each parameter for the

295 optimization process. Larger scales allow the MSPS to avoid getting stuck
 296 in local minima, and smaller scales help to refine the final solution. In each
 297 iteration, the MSPS algorithm dislocates in the search space using all pos-
 298 sible combinations of scales for all parameters, finds the optimal location,
 299 and moves to it. The process is repeated until the change observed in the
 300 function being optimized is below a set threshold. In this work, eight scales
 301 were found to be a reasonable compromise between processing time and the
 302 accuracy of the fit. The scales used in this work for each parameter are:
 303 $A(u) = \{0.01, 0.05, 0.1, 0.5, 1.0, 5.0, 10.0, 50.0\}$ *a.u.*, $\delta_t = \{0.001, 0.01,$
 304 $0.1, 1.0, 5.0, 10.0, 50.0, 100.0\}$ *ms*, $s = \{0.01, 0.05, 0.1, 0.5, 1.0, 2.0, 5.0,$
 305 $10.0\}$ s^{-1} , and $p = \{0.01, 0.05, 0.1, 0.5, 1.0, 2.0, 5.0, 10.0\}$ *ms*, which were
 306 defined considering the magnitude of the values observed in the results of the
 307 experiments reported by Okell et al. (Okell et al., 2010). The MSPS search
 308 space was additionally restricted in this work to avoid negative values for
 309 any parameter.

310 The MSPS search process minimizes the average absolute error (AAE)
 311 between the precalculated temporal signal curve using a set of blood flow
 312 parameters, and the discrete sample points for each voxel of the 4D ASL
 313 dataset. The AAE is preferred as a metric over the average sum of squared
 314 errors because fitting errors with values smaller than 1, which are common
 315 in these experiments, are assigned even smaller values when squared. In
 316 such a case, too small values might not be accurately represented due to
 317 physical limitations of the hardware being used for the experiments, and lead
 318 to erroneous parameter estimations. After identification of the optimal curve
 319 fitting parameters, the AAE between the estimated and ground-truth values
 320 for parameters $A(u)$, δ_t , s , and p is also calculated and averaged across all
 321 voxels in the binary segmentations in each scenario, for comparison purposes.

322 It should be noted that the AAE in this work serves two different pur-
 323 poses. First, it is used to optimize the fitting of a temporal curve to a set of
 324 discrete points. Second, it is used to compare true and estimated blood flow
 325 parameter values resulting from the experiments. In the following, AAE will
 326 refer only to its second function.

327 4. Results

328 Figure 5 shows axial maximum intensity projections of three frames from
 329 a real and a simulated 4D ASL MRA dataset. Both present the same vas-
 330 cular geometry, obtained from the same patient. The dynamics and disper-

331 sion of blood follows a similar pattern, but not exactly the same, as the
 332 real dataset depends on blood flow parameters of a specific subject, while
 333 the simulated datasets were generated using population average blood flow
 334 velocities, and assumed a blood flow model designed for 4D ASL MRA se-
 335 ries (Okell et al., 2010), which may not perfectly represent reality. In terms
 336 of the noise pattern, the homomorphic approach (Aja-Fernández et al., 2015)
 337 used to generate the noise is capable of capturing the more pronounced noise
 338 signal noticeable in real datasets in the central region of the brain, around
 339 the circle of Willis, compared to the border. This pattern is a consequence
 340 of the multi-coil acquisition of the datasets, and subsequent SENSE recon-
 341 struction, which can be difficult to simulate with other approaches (Phellan
 342 et al., 2018a).

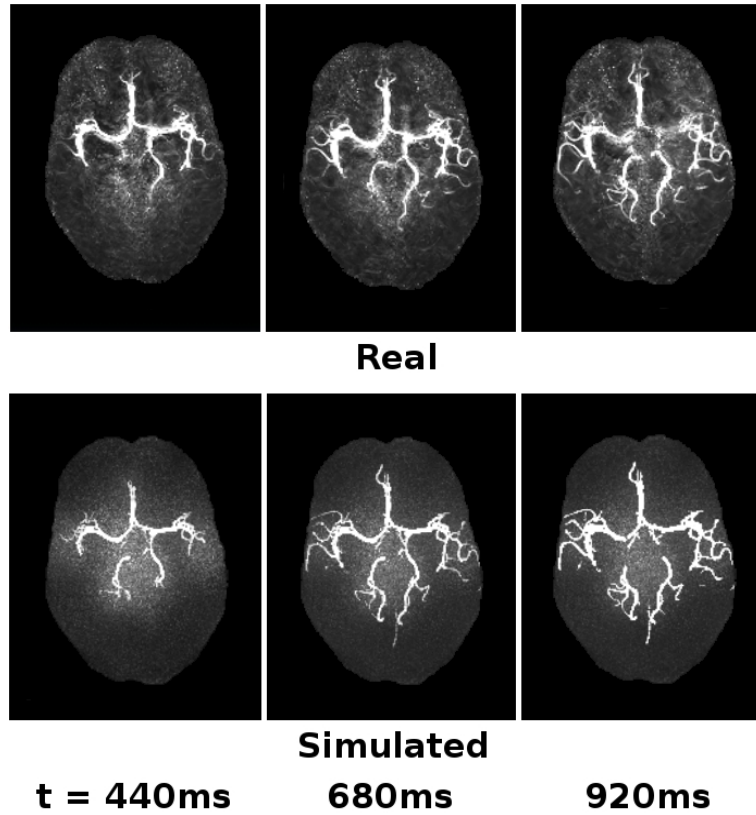


Figure 5: Maximum intensity projections of three images of real and simulated 4D ASL MRA datasets, for $t = 440$, 680 , and 920 ms (scenario 1).

343 With respect to the results of the method for quantitative blood flow
 344 parameters estimation, the resulting AAE for $A(u)$, δ_t , s , and p for each
 345 scenario are presented in the following tables. Table 3 shows the AAEs in
 346 arteries with a diameter larger or equal than 1 mm , and Table 4 shows the
 347 AAEs in arteries with a diameter smaller than 1 mm .

Scenario	$A(u)$ (<i>a.u.</i>)	δ_t (<i>ms</i>)	s (s^{-1})	p (<i>ms</i>)
1	4.74 ± 3.42	61.47 ± 51.03	2.14 ± 1.74	2.89 ± 1.91
2	5.21 ± 3.53	64.55 ± 58.66	2.23 ± 1.83	2.93 ± 2.01
3	5.64 ± 4.42	66.86 ± 58.20	2.85 ± 1.80	2.95 ± 2.09
4	5.43 ± 3.71	70.67 ± 56.41	2.76 ± 1.82	3.09 ± 2.00
5	4.52 ± 3.33	31.82 ± 19.70	1.89 ± 1.53	1.91 ± 1.22
6	5.00 ± 3.41	31.11 ± 24.99	1.99 ± 1.52	1.89 ± 1.48
7	4.99 ± 3.37	34.01 ± 24.62	1.98 ± 1.45	2.01 ± 1.16
8	5.29 ± 3.55	36.18 ± 22.77	2.11 ± 1.63	2.20 ± 1.58
9	4.13 ± 3.17	21.01 ± 13.62	0.93 ± 0.75	1.05 ± 0.92
10	4.23 ± 3.26	24.99 ± 14.80	0.93 ± 0.81	1.06 ± 0.81
11	4.45 ± 3.30	24.01 ± 14.75	0.98 ± 0.82	1.10 ± 0.81
12	4.79 ± 3.16	26.05 ± 16.66	0.97 ± 0.98	1.22 ± 0.85

Table 3: Average absolute error (AAE) between the estimated and ground-truth blood flow parameters in each scenario, for vessels with a diameter larger or equal than 1 mm . The optimal values in each column are in bold.

348 In general, it can be noticed that all blood flow parameters: $A(u)$, δ_t , s ,
 349 and p are more accurately estimated in case of large vessels, when compared
 350 to small vessels. It can also be noted that all blood flow parameters can be
 351 estimated with improved accuracy (measured by AAE) when the labeling
 352 time is set to its longest value of 3000 ms , which holds true for large and
 353 small vessels. Additionally, in each set of scenarios with the same labeling
 354 time: 1 to 4, 5 to 8, and 9 to 12, the AAE decreases when the temporal
 355 resolution r is increased, such that the lowest AAE is reached when r is
 356 set to 35 ms . This finding is also valid for both, small and large vessels.
 357 Consequently, the lowest AAE is reached when the blood is labeled for 3000
 358 ms and the datasets are acquired with a temporal resolution of 35 ms .

359 Nevertheless, some exceptions to these general trends can also be ob-
 360 served. The parameter $A(u)$ is estimated, in larger vessels, with a lower
 361 AAE in some scenarios with a labeling time of 300 ms (1 and 2), compared

Scenario	$A(u)$ (<i>a.u.</i>)	δ_t (<i>ms</i>)	s (s^{-1})	p (<i>ms</i>)
1	6.08 ± 6.36	73.84 ± 77.26	3.17 ± 2.83	3.19 ± 3.18
2	6.29 ± 6.02	75.43 ± 76.67	3.19 ± 2.49	3.47 ± 3.68
3	6.29 ± 6.07	74.58 ± 75.47	3.43 ± 2.35	3.53 ± 3.58
4	6.24 ± 6.99	82.71 ± 80.92	3.45 ± 2.44	3.68 ± 3.99
5	5.56 ± 4.25	47.19 ± 32.76	2.41 ± 1.63	2.23 ± 2.65
6	5.48 ± 4.23	47.89 ± 36.88	2.63 ± 1.74	2.31 ± 2.62
7	5.52 ± 4.27	45.24 ± 41.60	2.52 ± 1.55	2.50 ± 2.67
8	5.77 ± 4.59	54.63 ± 47.64	2.73 ± 1.86	2.52 ± 2.61
9	4.88 ± 3.63	26.00 ± 24.84	1.36 ± 0.80	1.28 ± 1.01
10	4.95 ± 3.65	27.05 ± 24.74	1.24 ± 0.77	1.29 ± 1.10
11	5.02 ± 3.78	29.37 ± 24.66	1.29 ± 0.84	1.33 ± 1.13
12	5.07 ± 3.84	30.93 ± 24.59	1.38 ± 0.79	1.46 ± 1.22

Table 4: Average absolute error (AAE) between the estimated and ground-truth blood flow parameters in each scenario, for vessels with a diameter smaller than 1 *mm*. The optimal values in each column are in bold.

to scenarios with a longer labeling time of 1000 *ms* (6, 7, and 8), independently of the temporal resolution. This is not the case for small vessels, where longer labeling times always lead to lower AAEs, for any parameter.

A second exception is that in some scenario sets using the same labeling time, the AAE does not always decrease when the temporal resolution is increased. This can be seen in large vessels in scenarios 4 and 7 for parameter $A(u)$; 6 and 11, for δ_t ; 4, 7, and 12 for s ; and 6 for p . The same result is present in small vessels in scenarios 3, 4, 6, and 7 for parameter $A(u)$; 3 and 7 for δ_t ; and 7, 10, and 11 for s . These exceptions do not seem to depend on the size of the vessel considered.

The final exception is that the lowest AAE is not reached in small vessels, for parameter s , when the blood is labeled for 3000 *ms* and the datasets are acquired with a temporal resolution of 35 *ms*, but when using a temporal resolution of 55 *ms*.

Figure 6 shows illustrations of estimated blood parameters from Scenario 9. Here, it becomes apparent that the parameters $A(u)$ and δ_t follow an expected behavior, with increased relative blood flow in large vessels, and early transit times in vessels closer to the neck. The parameter s also behaves as it is expected, because the large vessels closer to the labeling plane

are expected to presented lower dispersion of labeled blood than peripheral vessels, and lower dispersion is associated, in this case, with higher values of s . Generally, labeled blood disperses as it travels from the labeling plane to other peripheral regions of the cerebrovascular system (Okell et al., 2010). Finally, the estimated time-to-peak p presents a more noisy pattern, but it can be seen, in general, that vessels closer to the labeling plane are assigned a lower value of p , which is also associated with lower dispersion.

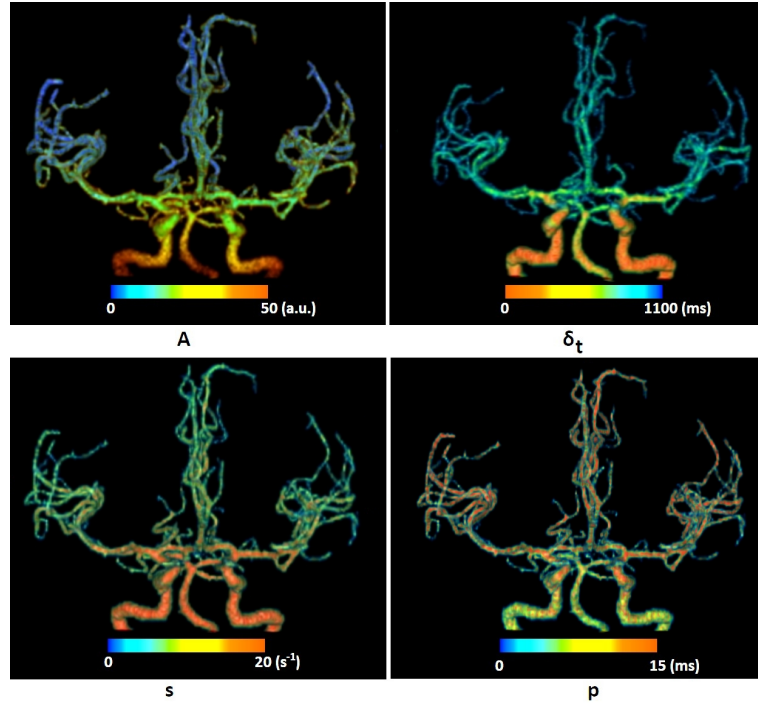


Figure 6: 3D visualizations of the estimated blood flow parameters in scenario 9 for one volunteer.

As a last consideration, the required time for acquisition of the 4D ASL MRA dataset in each scenario was determined by employing the corresponding acquisition parameters on the same scanner used to acquire the real 4D ASL MRA datasets used as reference in this project. The resulting acquisition times in minutes are: 19, 10, 7, 5, 29, 16, 11, 8, 82, 57, 33, 25 *min*, for scenarios 1 to 12, in that order. In general, it can be noticed that the acquisition time increases when higher temporal resolution and longer labeling times are used.

396 5. Discussion

397 The present paper describes a methodology for the generation of virtual
398 4D ASL MRA phantoms that uses real vascular geometries, a mathematical
399 model designed to describe the 4D ASL MRA signal of magnetically labeled
400 blood flowing through the arteries of the brain, and a homomorphic approach
401 to simulate spatially variant noise, present in images acquired with multiple
402 coils and SENSE reconstruction. Given the detailed control over the acquisition
403 parameters for the phantom generation, a use example was presented,
404 where the phantoms are employed to evaluate a method for blood flow parameters
405 estimation in multiple image acquisition scenarios. Each scenario
406 is created according to different settings described in the scientific literature
407 without having to scan participants multiple times on an MRI scanner, which
408 can be a time-consuming and expensive procedure.

409 The real 4D ASL MRA datasets acquired for reference purposes and the
410 virtual phantoms present the same vascular geometry, as the latter are based
411 on vascular segmentations obtained from high spatial resolution TOF MRA
412 images of the same volunteers, using a validated method (Forkert et al.,
413 2013). The blood flow dynamics are not exactly the same in corresponding
414 real and simulated datasets, but this is an expected result, as the underlying
415 blood flow velocities are different in both cases. In the real dataset, the blood
416 flow parameters correspond to a particular subject, while in the simulated
417 dataset, they are specified using population normative values (MacDonald
418 and Frayne, 2015; Zarrinkoob et al., 2015). Additionally, in case of small
419 vessels within the LPCA, RPCA, LMCA, and ACA regions, blood flow is
420 distributed equally at branching points, seeking to conserve the mass of blood
421 in the system. To the best of our knowledge, no publications have reported
422 the blood flow distribution in these small vessels, as small vessels are highly
423 variable in between subjects.

424 In terms of noise patterns, generating the virtual phantoms in 3D TOF
425 MRA space, and then resampling the datasets to the lower resolution 4D ASL
426 MRA space introduced partial volume effects, which are expected in a real
427 scenario. On the other hand, assuming a probabilistic distribution for noise,
428 such as the Rician distribution, is a common practice in literature (Gudbjartsson
429 and Patz, 1995). In particular, this work uses a homomorphic
430 approach (Aja-Fernández et al., 2015), which is capable of correctly simulating
431 the more pronounced noise signal noticeable in real datasets in the
432 central region of the brain, around the circle of Willis. This noise pattern is

433 a consequence of the multi-coil SENSE acquisition of the datasets, and can
 434 be difficult to simulate, as noted in our previous publication (Phellan et al.,
 435 2018a).

436 As it can be noted, the proposed methodology for 4D ASL MRA phantom
 437 creation is flexible enough to allow replacing any method used in the separate
 438 steps of the phantom generation, if needed, shown in Figure 1. In particular,
 439 considering that the phantoms were created and compared using data from
 440 healthy volunteers, the question of how well the 4D ASL MRA simulations
 441 would represent patients that present cardiovascular diseases still needs to be
 442 evaluated. The blood flow dynamics of patients that present disease can be
 443 represented by more complex models (Cebal et al., 2005), which could also be
 444 used in the proposed phantom generation methodology. Nevertheless, some
 445 other phenomena minimally present in healthy patients, such as motion of
 446 the subject during image acquisition, are not considered in the methodology.

447 The main advantage of the simulated datasets is that all acquisition and
 448 blood flow parameters can be controlled and used as a ground-truth for initial
 449 validation of medical image processing methods. Consequently, this work also
 450 shows an example where a method for blood flow parameter estimation is
 451 evaluated using the phantoms. It is observed that the relative blood volume,
 452 transit time, sharpness, and time to peak of the distribution that models
 453 the dispersion of magnetically labeled blood flowing through an artery can
 454 be more accurately estimated by the proposed method when the magnetic
 455 label is applied for a longer time. In particular, a long labeling time of
 456 3000 *ms* allows magnetically labeled blood to fill all arteries in a healthy
 457 brain before acquiring the 4D ASL MRA series, so that the magnitude of the
 458 measured signal acquired with such a long labeling time is decreasing with
 459 time, as labeled blood flushes out of the vascular system. This approach
 460 allows all time points of the curve that describe the signal evolution of any
 461 voxel corresponding to an artery to present non-zero values, which allows a
 462 more accurate blood flow model fitting.

463 In contrast to this finding, a labeling time of 300 *ms* implies that voxels
 464 corresponding to distal arteries present zero values in the initial sample points
 465 of their signal evolution curve. The more zero values a curve presents, the
 466 more difficult it is to optimize the curve fitting problem for the blood flow
 467 model used in this work. This happens because more than one combination
 468 of the blood flow parameters to be estimated in each scenario ($A(u)$, δ_t , s , and
 469 p) may lead to a result that closely represents the reference 4D ASL MRA
 470 signal, if it contains too many zero values, and it is difficult to discriminate

471 between them to identify the optimal combination of parameters.

472 For example, let's consider a peripheral artery section with a transit time
473 δ_t of 915 *ms*. Assuming a labeling time τ of 300 *ms*, and that images are
474 acquired from $t = 320$ *ms* to 920 *ms*, corresponding to scenario 4, with a
475 temporal resolution of 120 *ms*, the resulting signal curve will only contain
476 one non-zero value, e.g. $\{0.00, 0.00, 0.00, 0.00, 0.00, 1.88 \times 10^{-6}\}$. This
477 curve can be modelled with Equation 2, with considerably different blood
478 flow parameter configurations for $[A(u), \delta_t, s, p]$, e.g. [59, 915, 5, 9] and
479 [71, 915, 8, 8]. On the contrary, the same artery section, with a transit time
480 δ_t of 915 *ms*, but imaged using a labeling time of 1000 *ms*, with images
481 acquired from $t = 1015$ *ms* to 2095 *ms*, with temporal resolution of 120 *ms*,
482 corresponding to scenario 8, would generate the curve $\{0.25, 0.17, 0.11, 0.07,$
483 $0.05, 0.03, 0.02, 0.01, 0.00, 0.00\}$ for the parameter set [59, 915, 5, 9], and
484 $\{0.21, 0.14, 0.09, 0.06, 0.04, 0.03, 0.02, 0.01, 0.00, 0.00\}$ for the parameter
485 set [71, 915, 8, 8]. These last two curves present more non-zero values, which
486 allows improved hemodynamic model fitting to differentiate and select the
487 most accurate blood flow parameter configuration.

488 The results of this work also suggest that the temporal resolution is a
489 crucial parameter for accurate blood flow analysis in 4D ASL MRA datasets.
490 More precisely, all blood flow parameters are more accurately estimated with
491 higher temporal resolutions. Particularly, a temporal resolution of 35 *ms*
492 generates the lowest AAE in the evaluated scenarios, and the error increases
493 for the lower temporal resolutions of 50 *ms*, 90 *ms*, and 120 *ms*. The reason
494 for this finding can be ascribed to the higher number of images resulting
495 from a higher temporal resolution, which allows more accurate curve fitting
496 results and corresponding blood flow parameter estimations.

497 From the previous observations, it can be concluded that longer label-
498 ing times and higher temporal resolutions lead to more accurate estimations
499 using the evaluated blood flow parameter estimation method. This is a rea-
500 sonable conclusion that would also be expected if real annotated datasets
501 were used, showing the utility of the virtual phantoms for initial evaluation
502 of medical image processing methods. In this paper the use example focuses
503 on blood flow parameter estimation, within a previously segmented vascular
504 region. However, given that the virtual 4D ASL MRA phantoms have vas-
505 cular geometry and blood flow parameters ground-truth annotations, they
506 can also be used to evaluate methods that focus on vascular segmentation,
507 or combined segmentation and blood flow parameter estimation.

508 An additional aspect that needs to be considered is that in real scenarios,

509 increasing the temporal resolution leads to a lower signal-to-noise ratio (SNR)
 510 in later time points of a 4D ASL MRA dataset. In order to compensate
 511 for this loss in SNR, more images have to be acquired and averaged, thus,
 512 prolonging the total acquisition time. Consequently, it can be observed in the
 513 results of the experiments that using higher temporal resolutions to acquire
 514 the 4D ASL MRA datasets leads to longer acquisition times. Additionally,
 515 in this project, all scenarios with the same labeling time are also assigned
 516 the same TR independently of the temporal resolution. As an alternative
 517 that can be tested to generate the phantoms using the code available for this
 518 project (Phellan, 2019) the TR can be shortened as the temporal resolution
 519 increases. This modification will reduce the SNR of later time points as
 520 more imaging pulses are applied to the magnetically labeled blood, while
 521 potentially reducing the acquisition time of a 4D ASL MRA dataset.

522 Regarding the limitations of the proposed methodology, first, it assumes
 523 plug flow in the cerebrovascular system. However, the spatial resolution of
 524 4D ASL MRA datasets is not good enough for actually displaying laminar
 525 flow properties, so that it is believed that assuming plug flow does not rep-
 526 resent a practical limitation when analyzing real or simulated 4D ASL MRA
 527 datasets. Moreover, from a technical and theoretical perspective, simulating
 528 correct laminar flow properties would require a detailed computational fluid
 529 dynamics simulation of the whole vascular system, which is not feasible given
 530 the computational power requirements but also the need for a perfect ves-
 531 sel segmentation, even including microvascular structures (e.g. arterioles),
 532 which is not possible given current *in-vivo* imaging modalities.

533 Second, the proposed methodology assumes no mixing of blood occurs in
 534 the cerebrovascular system. Mixing of blood from different arteries practi-
 535 cally occurs mostly within the circle of Willis in the human brain. However,
 536 the circle of Willis is only partly developed in many people. Even if it is
 537 fully developed, there might be only minimal flow in healthy conditions. In
 538 order to fully account for possible mixing, one would also have to take into
 539 account leptomeninges as well as other collateral connections within the cere-
 540 broarterial system. Then, it would be very challenging to account for all of
 541 these factors correctly because it is not feasible to obtain sufficient *in-vivo*
 542 measurements of the exact properties. However, in healthy subjects blood
 543 mixing and blood flow through other collateral connections are known to have
 544 a rather small effect compared to the blood flow from the major arteries.

545 6. Conclusion

546 In conclusion, this work presented a method to generate simulations of
547 4D ASL MRA annotated datasets. The annotations include ground truth
548 data of the vascular geometry and blood flow parameters of each dataset.
549 The annotated simulations can be used to evaluate medical image process-
550 ing methods. In particular, this work presented a use example, where the
551 phantoms were used to measure the accuracy of a blood flow parameter esti-
552 mation method in various scenarios with different acquisition parameters. It
553 was noticed that the blood flow parameters were more accurately estimated
554 when the blood is magnetically labeled for longer times, and the datasets are
555 acquired with a higher temporal resolution, as it would be expected if real
556 annotated datasets were employed.

557 Acknowledgements

558 This work was supported by Natural Sciences and Engineering Research
559 Council of Canada (NSERC), Hotchkiss Brain Institute (HBI), and Alberta
560 Innovates. Dr. Nils D. Forkert is funded by Canada Research Chairs. Dr.
561 Alexandre X. Falcão thanks CNPq 302970/2014-2 and FAPESP 2014/12236-
562 1.

563 Conflict of interest

564 The authors declared no potential conflicts of interest with respect to
565 the research, authorship, and/or publication of this article. Michael Helle
566 is employed by Philips Research. Thomas W. Okell is the author of a US
567 patent licensed to Siemens Healthcare that aims to quantify blood flow rates
568 from angiographic data, which relies upon a kinetic model such as that used
569 in this study.

570 References

- 571 Aja-Fernández, S., Pie, T., Vegas-Sánchez-Ferrero, G., et al., 2015. Spatially
572 variant noise estimation in MRI: A homomorphic approach. *Medical image*
573 *analysis* 20, 184–197.
- 574 Aja-Fernández, S., Vegas-Sánchez-Ferrero, G., Tristán-Vega, A., 2014. Noise
575 estimation in parallel MRI: GRAPPA and SENSE. *Magnetic resonance*
576 *imaging* 32, 281–290.

577 Cebal, J.R., Castro, M.A., Burgess, J.E., Pergolizzi, R.S., Sheridan, M.J.,
578 Putman, C.M., 2005. Characterization of cerebral aneurysms for assess-
579 ing risk of rupture by using patient-specific computational hemodynamics
580 models. *American journal of neuroradiology* 26, 2550–2559.

581 Cocosco, C.A., Kollokian, V., Kwan, R.K.S., Pike, G.B., Evans, A.C., 1997.
582 Brainweb: Online interface to a 3D MRI simulated brain database, in:
583 *NeuroImage*, Citeseer. p. 1.

584 Department of information, evidence and research of the World Health Or-
585 ganization, 2017. WHO methods and data sources for country-level causes
586 of death 2000–2015. Report No. 2016.3, Geneva .

587 Falcão, A.X., Stolfi, J., de Alencar Lotufo, R., 2004. The image foresting
588 transform: Theory, algorithms, and applications. *IEEE transactions on*
589 *pattern analysis and machine intelligence* 26, 19–29.

590 Forkert, N., Säring, D., Fiehler, J., Illies, T., Möller, D., Handels, H., 2009.
591 Automatic brain segmentation in Time-of-Flight MRA images. *Methods*
592 *of information in medicine* 48, 399–407.

593 Forkert, N.D., Fiehler, J., Ries, T., Illies, T., Möller, D., Handels, H., Säring,
594 D., 2011. Reference-based linear curve fitting for bolus arrival time estima-
595 tion in 4D MRA and MR perfusion-weighted image sequences. *Magnetic*
596 *resonance in medicine* 65, 289–294.

597 Forkert, N.D., Schmidt-Richberg, A., Fiehler, J., Illies, T., Möller, D., Säring,
598 D., Handels, H., Ehrhardt, J., 2013. 3D cerebrovascular segmentation
599 combining fuzzy vessel enhancement and level-sets with anisotropic energy
600 weights. *Magnetic resonance imaging* 31, 262–271.

601 Gudbjartsson, H., Patz, S., 1995. The Rician distribution of noisy MRI data.
602 *Magnetic resonance in medicine* 34, 910–914.

603 Hagen, G., 1839. Ueber die Bewegung des Wassers in engencylindrischen
604 Röhren. *Annalen der Physik* 122, 423–442.

605 Hamarneh, G., Jassi, P., 2010. VascuSynth: simulating vascular trees for
606 generating volumetric image data with ground-truth segmentation and tree
607 analysis. *Computerized medical imaging and graphics* 34, 605–616.

- 608 Kiepas, P., Sieradzki, J., 2015. MRI homomorphic noise estimation. <https://github.com/quepas/mri-homomorphic-noise-estimation>. Accessed:
609 2018-12-28.
610
- 611 Kopeinigg, D., Bammer, R., 2014. Time-resolved angiography using inflow
612 subtraction (TRAILS). *Magnetic resonance in medicine* 72, 669–678.
- 613 Lu, H., Clingman, C., Golay, X., Van Zijl, P.C., 2004. Determining the
614 longitudinal relaxation time (T1) of blood at 3.0 Tesla. *Magnetic resonance
615 in medicine* 52, 679–682.
- 616 MacDonald, M.E., Frayne, R., 2015. Phase contrast MR imaging measure-
617 ments of blood flow in healthy human cerebral vessel segments. *Physio-
618 logical measurement* 36, 1517.
- 619 Miraucourt, O., Salmon, S., Szopos, M., Thiriet, M., 2017. Blood flow in the
620 cerebral venous system: Modeling and simulation. *Computer methods in
621 biomechanics and biomedical engineering* 20, 471–482.
- 622 Okell, T.W., Chappell, M.A., Schulz, U.G., Jezzard, P., 2010. A kinetic
623 model for vessel-encoded dynamic angiography with arterial spin labeling.
624 *Magnetic resonance in medicine* 64, 698–706.
- 625 Phellan, R., 2019. Four-dimensional arterial spin labeling MR
626 angiography virtual phantoms. [https://github.com/rphellan/
627 4DASLMRAVirtualPhantoms](https://github.com/rphellan/4DASLMRAVirtualPhantoms). Accessed: 2019-05-22.
- 628 Phellan, R., Forkert, N.D., 2017. Comparison of vessel enhancement algo-
629 rithms applied to time-of-flight MRA images for cerebrovascular segmen-
630 tation. *Medical physics* 44, 5901–5915.
- 631 Phellan, R., Linder, T., Helle, M., Spina, T.V., Falcão, A., Forkert, N.D.,
632 2018a. Four-Dimensional ASL MR Angiography Phantoms with Noise
633 Learned by Neural Styling, in: *Intravascular Imaging and Computer As-
634 sisted Stenting and Large-Scale Annotation of Biomedical Data and Expert
635 Label Synthesis*. Springer, pp. 131–139.
- 636 Phellan, R., Lindner, T., Helle, M., Falcão, A.X., Forkert, N.D., 2018b.
637 Automatic temporal segmentation of vessels of the brain using 4D ASL
638 MRA images. *IEEE transactions on biomedical engineering* 65, 1486–1494.

- 639 Poiseuille, J.L., 1844. Recherches expérimentales sur le mouvement des liq-
640 uides dans les tubes de très-petits diamètres. Imprimerie Royale.
- 641 Robson, P.M., Dai, W., Shankaranarayanan, A., Rofsky, N.M., Alsop, D.C.,
642 2010. Time-resolved vessel-selective digital subtraction MR angiography
643 of the cerebral vasculature with arterial spin labeling. *Radiology* 257, 507–
644 515.
- 645 Ruppert, G.C., Chiachia, G., Bergo, F.P., Favretto, F.O., Yasuda, C.L.,
646 Rocha, A., Falcão, A.X., 2017. Medical image registration based on water-
647 shed transform from greyscale marker and multi-scale parameter search.
648 *Computer methods in biomechanics and biomedical engineering: Imaging*
649 *& visualization* 5, 138–156.
- 650 Zarrinkoob, L., Ambarki, K., Wåhlin, A., Birgander, R., Eklund, A., Malm,
651 J., 2015. Blood flow distribution in cerebral arteries. *Journal of cerebral*
652 *blood flow and metabolism* 35, 648–654.